Adiabatic and Nonadiabatic State-to-State Quantum Dynamics for $O(^1D) + H_2(X^1\Sigma_g^+, v_i = j_i = 0) \rightarrow OH(X^2\Pi, v_f, j_f) + H(^2S)$ Reaction†

Shi Ying Lin and Hua Guo*

Department of Chemistry and Chemical Biology, University of New Mexico, Albuquerque, New Mexico 87131

Received: December 11, 2008; Revised Manuscript Received: February 16, 2009

The authors report accurate quantum dynamics calculations for the title reaction on the three lowest electronic state potentials. The adiabatic pathway on the ground electronic state ($1^1A'$) of H_2O has a complex-forming mechanism, manifested by rotationally hot and vibrationally cold OH products with a nearly forward−backward symmetric angular distribution. As energy increases, the adiabatic pathway via the $1^1A''$ state and nonadiabatic pathway via the $2^1A'$ state become significant. The former has an abstraction mechanism and produces an exclusively backward differential cross section. On the other hand, the latter has essentially the same dynamic signatures of the ground-state pathway. The inclusion of the two excited-state pathways is necessary to quantitatively reproduce the observed rise in the integral cross section at high energies and the increasingly backward bias in the differential cross section. It is also found that the inclusion of the excited-state dynamics, particularly the nonadiabatic $2^1A'$ pathway, greatly improves the agreement with the measured rate constant.

1. Introduction

The exoergic reaction between the excited oxygen atom, $O(^1D)$, and hydrogen molecule is known to play an important role in many gas phase processes in the atmosphere[1] and in combustion.[2] For these reasons, it has been extensively studied.[3] It is well-established that the interaction between $O(^1D)$ and $H_2(X^1\Sigma_g^+)$ results in five singlet states.[4−7] In particular, a Σ state, a doubly degenerate Π state, and a doubly degenerate Δ state in linearity give rise to three $^1A'$ and two $^1A''$ states in C_s symmetry. Among them, only three are relevant to the title reaction because the Δ doublet is strongly repulsive. As shown in Figure 1, the ground electronic state ($1^1A'$) of H_2O correlates adiabatically from the $O(^1D) + H_2(X^1\Sigma_g^+)$ reactant channel to the $OH(X^2\Pi) + H(^2S)$ product channel via a barrierless insertion pathway.[4,6] Indeed, the corresponding reactive process is considered as a prototype for insertion reactions, which, unlike a direct abstraction reaction such as the $H + H_2$ reaction, is dominated by a long-lived reaction intermediate supported by the deep H_2O potential well.[3,8−11] Such a complex-forming mechanism manifests itself by vibrationally cold and rotationally hot products as well as a forward−backward symmetric differential cross section (DCS), as suggested by the statistical theory.[12,13]

In addition to the reaction pathway on the ground $1^1A'$ state, there are two other pathways via excited electronic states of the H_2O system, as shown in Figure 1. The first is an adiabatic pathway on the $1^1A''$ state potential energy surface (PES), which also correlates with the $OH(X^2\Pi) + H(^2S)$ product channel. Unlike the $1^1A'$ state, however, the $1^1A''$ PES has no potential well and is dominated by an abstraction barrier of approximately 0.1 eV (2.3 kcal/mol) near the entrance channel.[5−7] As a result, the dynamics on the $1^1A''$ state PES is direct and fast, in sharp contrast with the complex-forming reaction on the ground $1^1A'$ state PES. Its dynamical signatures, such as an asymmetric DCS, are thus easily identifiable.

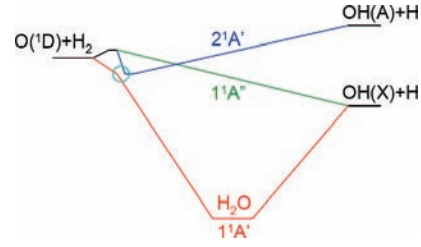

Figure 1. Schematic potential energy surfaces for the three reaction pathways. The circle indicates the conical intersection between the two $^1A'$ states.

Finally, there is a nonadiabatic pathway via the excited $2^1A'$ state, which correlates adiabatically with the excited product channel ($OH(A^2\Sigma^+) + H(^2S)$), as shown in Figure 1. Its contribution to the title reaction stems from nonadiabatic transitions through a conical intersection to the lower $1^1A'$ state. Interestingly, the $2^1A'$ state also has a collinear barrier of ~0.1 eV near the entrance channel,[6,7] because it and the $1^1A''$ state form a doubly degenerate Π state in linearity. The contribution of this nonadiabatic pathway cannot be easily determined experimentally because the curve crossing occurs early in the reaction path immediately after the barrier, and the dynamics is thus quite similar to that on the ground electronic state. For this reason, theoretical analysis is essential to delineate its contribution to the reaction.

Since both excited states have small barriers, the reaction pathway via the ground electronic state ($1^1A'$) dominates at low energies. Indeed, such a picture is consistent with the lack of strong temperature dependence of the rate constant.[14−17] The dominance of the complex-forming mechanism at low collision energies was further confirmed by experimental observations of a near forward−backward symmetric DCS, a highly excited product rotational distribution, and a monotonically decaying product vibrational distribution.[18−29] Numerous theoretical studies have been reported on the adiabatic insertion reaction on the $1^1A'$ state, and the agreement with the low-energy experimental data is generally satisfactory.[20,22,24,29−43] Very recently,

† Part of the "George C. Schatz Festschrift".

* E-mail: hguo@unm.edu.

10.1021/jp810948k CCC: $40.75
Published on Web 03/11/2009

we have reported state-resolved quantum mechanical DCS for the $1^1A'$ state reaction over a large energy range.[44]

On the other hand, recent experimental studies have suggested that the participation of excited states becomes non-negligible above 0.1 eV of collision energy. The evidence includes a rising integral cross section (ICS), a buildup of a backward bias in the DCS, and vibrational excited OH products at higher collision energies.[20,22,27,40,45−51] Theoretical studies, including surface-hopping quasi-classical trajectory (QCT) calculations[51−56] and limited quantum mechanical studies,[37,40,56−60] offered support for this conjecture concerning the participation of the excited states. However, the conventional QCT approach is not expected to provide quantitatively accurate results due to its arbitrariness in treating the quantum effects. Indeed, significant discrepancies have been reported between the calculated and measured ICSs.[59] In addition, the surface hopping model for treating nonadiabatic transitions is still not universally proven, and the inclusion of excited states in QCT calculations did not lead to a quantitative agreement with experimental data.[40,54,56] On the other hand, quantum dynamical studies of the nonadiabatic excited-state pathway either were limited to $J = 0$,[58,60] or used dynamical simplifications, such as the coupled-state approximation.[59] Furthermore, no state-to-state attribute has been calculated for the nonadiabatic reaction pathway, although quantum mechanical reaction probabilities[37] and cross sections[40,41,56] have been reported for the adiabatic $1^1A''$ pathway, which is much easier to treat quantum mechanically.

Given the importance of this prototypic system, a uniformly accurate treatment of all three reaction pathways is highly desired to provide a quantitative understanding of the title reaction. In this publication, we report a definitive quantum mechanical characterization of the reaction dynamics for this reaction, including all three pathways. Such an endeavor is highly desired because of the presence of quantum effects, such as tunneling, zero-point energy, resonances, and nonadiabatic transitions. However, the quantum dynamical calculations involving the ground $1^1A'$ state and the coupled excited $2^1A'$ state present a considerable challenge because of the large basis needed to cover the deep H_2O well and the large number of partial waves due to the barrierless pathway. Nonadiabatic transitions further compound the difficulties. To overcome these obstacles, our quantum dynamical calculations were performed using an efficient and accurate Chebyshev propagator[61,62] with no dynamic approximations. State-to-state reaction probabilities, excitation functions, integral and differential cross sections, and rate constant were obtained on the highly accurate Dobbyn−Knowles (DK) PESs,[6,7] which include all three lowest-lying singlet electronic states of H_2O as well as the nonadiabatic coupling between the two $^1A'$ states. As shown below, the quantum mechanical calculations yielded quantitative agreement with experimental measurements, underscoring substantial improvements over previous theoretical models. These results not only provide a deeper understanding of the reaction dynamics but also serve as a benchmark for more approximate treatments of the dynamics. This paper is organized as follows. The next section (Section 2) outlines theoretical methods for calculating both ICS and DCS. The results are presented and discussed in Section 3. Concluding remarks are given in Section 4.

2. Theory

A.. Adiabatic and Nonadiabatic Quantum Dynamics. The Chebyshev wave packet method[61,62] was used to investigate both the adiabatic and nonadiabatic quantum dynamics of the title reaction. Since the details of this method are well-documented,[44,63,64] only a brief outline is given here. Essentially, initial Gaussian wave packets associated with a prespecified reactant internal state were propagated using the Chebyshev three-term recursion relation, which entails the multiplication of the Hamiltonian matrix onto the Chebyshev wave packet vector. Projections onto product internal states were then made in the product channel, and scattering attributes were extracted. This approach is similar to the real wave packet method of Gray and Balint-Kurti.[65]

For adiabatic dynamics on the $1^1A'$ or $1^1A''$ state, the Hamiltonian for the title reaction can be expressed in the product Jacobi coordinates (R, r, γ) as follows ($\hbar = 1$):

$$\hat{H} = \hat{T} + V(R, r, \gamma) = -\frac{1}{2\mu_R}\frac{\partial^2}{\partial R^2} - \frac{1}{2\mu_r}\frac{\partial^2}{\partial r^2} + \frac{\hat{j}^2}{2\mu_r r^2} + \frac{\hat{l}^2}{2\mu_R R^2} + V(R, r, \gamma) \quad (1)$$

where μ_R and μ_r are the corresponding reduced masses for the radial Jacobi coordinates, and $V(R, r, \gamma)$ is the PES of the corresponding electronic state. The OH product was approximated as a closed-shell species by ignoring its electronic and spin angular momenta. Hence, the square of the orbital angular momentum operator, $\hat{l}^2$ can be further expressed as

$$\hat{l}^2 \equiv (\hat{J} - \hat{j})^2 = \hat{J}^2 + \hat{j}^2 - 2\hat{J}_z\hat{j}_z - \hat{J}_+\hat{j}_- - \hat{J}_-\hat{j}_+ \quad (2)$$

in which $\hat{J}$ and $\hat{j}$ are, respectively, the total and diatomic angular momentum operators with $\hat{J}_z$ and $\hat{j}_z$ as their projections onto the body-fixed (BF) z-axis; namely, the R vector. $\hat{J}_+(\hat{J}_-)$ and $\hat{j}_+(\hat{j}_-)$ are the corresponding raising (lowering) operators. As in our recent work,[44] the Coriolis coupling derived from the last two terms in eq 2, which is known to be important for the title reaction,[38] was fully accounted for. It should be noted that the $1^1A'$ pathway actually couples with the excited $2^1A'$ state. In this work, however, this nonadiabatic coupling was ignored, and the dynamics was treated as adiabatic.

The $2^1A'$ electronic state contributes to the reaction via a nonadiabatic interaction with the ground $1^1A'$ state near the conical intersection. The corresponding Hamiltonian is given in a diabatic representation:

$$\hat{H} = \hat{T} + \begin{pmatrix} V_\Sigma & V_{\Sigma\Pi} \\ V_{\Sigma\Pi} & V_\Pi \end{pmatrix} \quad (3)$$

where the same kinetic energy operator (KEO) in eq 1 was used. The diagonal terms in the DK potential matrix[6,7] represent the diabatic PESs for the Σ and Π states, respectively, and the off-diagonal term, $V_{\Sigma\Pi}$, represents the nonadiabatic coupling. Diagonalization of the 2×2 diabatic PES matrix yielded two adiabatic PESs for the $1^1A'$ and $2^1A'$ states. The corresponding wave packet was decomposed accordingly into two components:

$$\Psi = \begin{pmatrix} \psi_\Sigma \\ \psi_\Pi \end{pmatrix} \quad (4)$$

and the calculation of the action of the Hamiltonian, $\hat{H}\Psi$, is straightforward:

$$\hat{H}\Psi = \begin{pmatrix} (\hat{T} + V_{\Sigma})\psi_{\Sigma} + V_{\Sigma\Pi}\psi_{\Pi} \\ (\hat{T} + V_{\Pi})\psi_{\Pi} + V_{\Sigma\Pi}\psi_{\Sigma} \end{pmatrix} \quad (5)$$

The Hamiltonian and wave packet were discretized in a mixed representation, consisting of a direct product discrete variable representation for the two radial degrees of freedom (R, r) and a finite basis representation for the angular degrees of freedom.[66] Actions of the radial KEOs onto the wave packet were efficiently evaluated using the fast sine-Fourier transform (sine-FFT) method.[67] On the other hand, a parity-adapted basis was used for the angular degrees of freedom,

$$|j\Omega;Jp\rangle = (2 + 2\delta_{\Omega,0})^{-1/2}(|J\Omega\rangle|j\Omega\rangle + p(-1)^{J}|J - \Omega\rangle|j - \Omega\rangle) \quad (6)$$

where $|j\Omega\rangle \equiv \Theta_{j\Omega}(\gamma, 0)$ are normalized associate Legendre functions with the Condon−Shortley phase convention,[68] and $|J\Omega\rangle = \sqrt{[(2J + 1)/(8\pi^2)]}D^{J*}_{\Omega,0}$ represents the overall rotation, where $D^{J}_{\Omega,M}$ is the Wigner rotation matrix.[69] The parity adaptation reduced the basis size almost by half as the helicity quantum number (i.e. the projection of J and j onto the BF z-axis, Ω) is restricted to be non-negative. On this basis, the rotational KEOs in eq 2 are either diagonal or tridiagonal, and thus, actions of these terms onto the wave packet can be evaluated in a straightforward manner.

To calculate the action of the potential energy operator, the following pseudospectral transformation was used to convert the wave packet from the angular FBR to a grid:[70,71]

$$T^{(\Omega)}_{j\beta} = \sqrt{w_{\beta}}\Theta_{j\Omega}(\gamma_{\beta}) \quad (7)$$

where β denotes the index of the Gauss−Legendre quadrature points for the internal (Jacobi) angular coordinate and w_{β} is the corresponding weight.

B. Differential and Integral Cross Sections. The state-to-state S-matrix elements are the building blocks of all observable scattering attributes. In this work, they were extracted from the Chebyshev wave packet using a method proposed by us recently.[64] In addition to the vibrational (v) and rotational (j) quantum numbers, an additional quantum number is needed to specify the asymptotic quantum states, which could be either the orbital angular momentum quantum number, l, or the helicity quantum number, Ω. The former was used in this work, and thus, the state-to-state S-matrix elements are denoted as $S^{Jp}_{v_f j_f l_f \leftarrow v_i j_i l_i}(E)$. This l-labeled S-matrix can be easily transformed to the Ω-labeled one as

$$S^{Jp}_{v_f j_f \Omega_f \leftarrow v_i j_i \Omega_i} = \sum_{l_i l_f} \left(U^{Jpj_f}_{l_f \Omega_f}\right)^{*} S^{Jp}_{v_f j_f l_f \leftarrow v_i j_i l_i} U^{Jpj_i}_{l_i \Omega_i} \quad (8)$$

where the transformation matrix is given by[72]

$$U^{Jpj}_{l\Omega} = \frac{i^{l}}{\sqrt{2(1 + \delta_{\Omega,0})}}\left[\left\langle j\Omega, J - \Omega \middle| l0 \right\rangle + p(-1)^{J}\left\langle j - \Omega, J\Omega \middle| l0 \right\rangle\right] \quad (9)$$

with $\langle ..,..|l..\rangle$ denoting the Clebsch-Gordan coefficients.[69]

The state-to-state differential cross section (DCS) was calculated using the following formula:[72]

$$\frac{d\sigma_{v_f j_f, v_i j_i}}{d\Omega}(\theta, E) = \frac{1}{8k^2_{v_i j_i}}\frac{1}{(2j + 1)}\sum_{\Omega_f \Omega_i}\left[\left|f_{+}(\theta, E)\right|^2 + \left|f_{-}(\theta, E)\right|^2\right] \quad (10)$$

where

$$f_{+}(\theta, E) = \sum_{Jp}(2J + 1)\, d^{J}_{\Omega_f \Omega_i}(\pi - \theta)\, S^{Jp}_{v_f j_f \Omega_f \leftarrow v_i j_i \Omega_i}(E) \quad (11a)$$

$$f_{-}(\theta, E) = \sum_{Jp} p(2J + 1)\, d^{J}_{\Omega_f \Omega_i}(\theta)\, S^{Jp}_{v_f j_f \Omega_f \leftarrow v_i j_i \Omega_i}(E) \quad (11b)$$

where θ is the center of mass scattering angle and $d^{J}_{\Omega_f \Omega_i}(\theta)$ is a reduced rotation matrix element.[69]

The state-to-state integral cross section (ICS) was obtained as follows:

$$\sigma_{v_f j_f, v_i j_i}(E) = \frac{\pi}{(2j_i + 1)k^2_{v_i j_i}}\sum_{J,p,l_i,l_f}(2J + 1)\left|S^{Jp}_{v_f j_f l_f \leftarrow v_i j_i l_i}(E)\right|^2 \quad (12)$$

where, $k^2_{v_i j_i} = 2\mu_R(E - E_{v_i j_i})$ and $E_{v_i j_i}$ is the rovibrational internal energy of the initial reactant state.

C. Total Reaction Cross Section and Rate Constant. The calculation of state-to-state S-matrix elements is very expensive computationally. If the total reaction cross section is the only desired attribute, it can be obtained much less expensively using a flux method.[73,74] To save computational time, we limited S-matrix calculations to low-J partial waves, which allowed the convergence of the DCS up to about 0.15 eV of collision energy. The flux method was used to calculate total reaction probabilities for high-J partial waves, which allowed the total reactive ICS to converge at a higher collision energy of 0.34 eV. The results of the two types of calculations have been compared at certain intermediate J values, and they agreed very well with each other.

There are some differences between the implementations of the two methods. For example, the product (H−OH) Jacobi coordinates were used in the S-matrix calculations to facilitate projections to the product internal states, whereas the reactant (O−H_2) Jacobi coordinates were used in the flux calculations. The permutation symmetry in H_2 allows additional savings in the latter approach. In addition, the flux calculations required a smaller grid because no final state needs be resolved.

The initial state-specified rate constant can be obtained by Boltzmann-averaging the corresponding ICS over the collision energy (E_c):

$$k_{v_i j_i}(T) = \frac{f}{k_B T}\left(\frac{8}{\pi\mu_R k_B T}\right)^{1/2}\int_0^{\infty}\sigma_{v_i j_i}(E_c)\, e^{-E_c/k_B T}E_c\, dE_c \quad (13)$$

where k_B is the Boltzmann constant, T is temperature, and $f = 1/5$ is the electronic degeneracy factor of the reactant channel.

TABLE 1: Numerical Parameters Used in the Direct Total Probability Calculations Using a Flux Method[a]

	$1^1A'$ and $1^1A''$	$2^1A'$
grid/basis range and size	$R \in (10^{-16}, 14)(N_R = 224)$ $r \in (0.5, 8.0)(N_r = 63)$ even j from 0 to $j_{max} = 48$ $(N_\gamma = 25$ over $\gamma \in (0, 90°))$	$R \in (10^{-16}, 14)(N_R = 224)$ $r \in (0.5, 11.0)(N_r = 89)$ even j from 0 to $j_{max} = 54$ $(N_\gamma = 28$ over $\gamma \in (0, 90°))$
damping	$e^{-0.002\times(R-11)^2}$ for $R > 11$ $e^{-0.005\times(r-5)^2}$ for $r > 5$ $= 1$ otherwise	$e^{-0.002\times(R-11)^2}$ for $R > 11$ $e^{-0.005\times(r-8)^2}$ for $r > 8$ $= 1$ otherwise
initial wave packet $(e^{-((R-R_0)/\delta)^2/2}\cos(k_0R))$	$R_0 = 9.0$ $E_0 = (\hbar^2k_0^2)/(2\mu) = 0.4$ eV $\delta = 0.15$	same as left
spectral control	energy cut of 0.5 hartree (PES and each rotational kinetic energy term)	same as left
position where the flux calculated	$r_{flux} = 4.9$	$r_{flux} = 7.9$
propagation steps	15k for $1^1A'$ and 5k for $1^1A''$	20k

[a] Atomic units used unless specified explicitly; R, r, γ stand for the reactant Jacobi coordinates.

Finally, the contributions from all three electronic states were summed together to obtain the final results for the scattering attributes, such as the DCS, ICS, and rate constant.

3. Results and Discussion

The S-matrix calculations were carried out for all three reaction pathways to converge the initial state ($v_i = j_i = 0$) specified and final state resolved DCSs up to 0.15 eV of collision energy. The DCSs for the reactive scattering on the $1^1A'$ ground electronic state have already been reported for the first 31 ($J = 0-30$) partial waves in our previous work.[44] For the $1^1A''$ and $2^1A'$ pathways, 21 ($J = 0-20$) and 31 ($J = 0-30$) partial waves, respectively, were needed to converge the DCSs in the same collision energy range. The numerical parameters used for the $2^1A'$ nonadiabatic scattering dynamics were identical to those used in previous work for the $1^1A'$ pathway (see Table 1 of ref 44). For the $1^1A''$ calculations, a slightly larger basis size was chosen to converge some very small state-to-state attributes. The numbers if grid points for both radial Jacobi coordinates, R and r, were increased to 199, while the angular basis was increased to 120 ($j_{max} = 119$). On the other hand, only 5000 Chebyshev propagation steps were required for this pathway due to its fast abstraction dynamics.

To obtain the rate constant at higher temperatures, we have augmented the S-matrix calculations at low J values with the less expensive flux calculations of the total reaction probabilities at higher J values. In particular, we carried out additional flux calculations for higher partial waves ($J = 31-40$) for the $1^1A'$ pathway, which allowed the convergence of the total ICS up to ~0.34 eV of collision energy and the rate constant up to ~500 K. Similarly, total reaction probabilities for the $1^1A''$ and $2^1A'$ pathways were obtained using the same flux approach with $J = 21-40$ and $31-40$ partial waves, respectively, which allowed the same level of convergence. The numerical parameters used in the flux calculations are summarized in Table 1. Interestingly, in the nonadiabatic dynamical calculations, we had to move the position of the dividing surface in the flux calculation to a much larger O−H distance, $r_f = 7.9\ a_0$, from $r_f = 4.9\ a_0$ used in the single surface dynamics calculations,[44] to converge the probabilities, indicating the nonadiabatic interaction is quite strong.

A. Total Reaction Probability, Integral Cross Section, and Rate Constant. In Figure 2, the total reaction probabilities for several selected partial waves were displayed for three reaction pathways. As the figure shows, the reaction is dominated by the adiabatic $1^1A'$ pathway, but contributions from the other two excited electronic pathways are nonzero. Even at low collision energies, the nonadiabatic $2^1A'$ reaction probabilities are nonnegligible. On the other hand, the adiabatic $1^1A''$ pathway starts to contribute only above ~0.1 eV of collision energy, due apparently to the entrance channel potential barrier. The contributions of the excited electronic states increase sharply with increasing collision energy.

Due to the barrierless reaction path of the ground $1^1A'$ state, its $J = 0$ probability shows no threshold. However, a threshold begins to emerge for nonzero J values and increases with J due to the centrifugal potential energy barrier. In addition, the energy dependence of the probabilities shows oscillatory structure, due apparently to metastable resonances supported by the deep H_2O well. However, these resonance features are quite broad, indicating relatively long lifetimes, as observed in earlier calculations.[30,35,43]

For the $1^1A''$ pathway, the total reaction probabilities show strikingly different characteristics from those on the ground $1^1A'$ state. The $J = 0$ reaction probability has a nonzero threshold, and the probability increases smoothly with energy. This is due to the fact that this electronic state is dominated by a collinear reaction path with a small potential barrier in the entrance channel. As a result, the reaction has an appreciable probability only above the barrier. For high J values, the threshold increases to higher energies as the barrier is raised by the centrifugal term.

The characteristics of the $2^1A'$ reaction pathway are somewhere between the two extremes. The energy dependence of the total reaction probabilities is oscillatory and generally increases with energy. Despite the potential barrier on the $2^1A'$ state PES, the $J = 0$ shows no threshold. This is because the reaction takes place via nonadiabatic transitions to the $1^1A'$ state, which has a barrierless pathway. The $2^1A'$ threshold for higher J values follows closely with that of the $1^1A'$ state.

The energy dependence of the total ICS is displayed in Figure 3 and compared with experimental and other theoretical results. As expected, the ICS is dominated by the ground $1^1A'$ state pathway in the entire energy range. However, contributions from the two excited-state pathways are quite significant, particularly at high collision energies. These contributions are responsible for the unusual energy dependence of the total ICS, which first decreases with the collision energy until reaching a minimum at about 0.09 eV and then slowly increases. The breakdown of contributions from the three pathways clearly indicates that the rising of the ICS at higher energies stems from the excited electronic pathways, because the ICS from the adiabatic $1^1A'$ pathway is a monotonic decaying function of the collision energy. This is consistent with the trend observed by Liu and

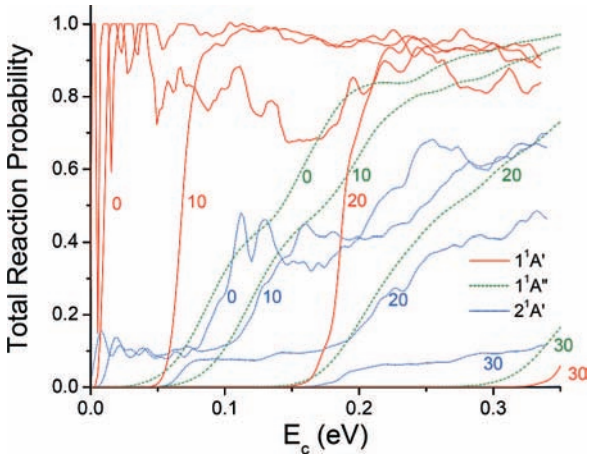

Figure 2. Total reaction probabilities for $J = 0$, 10, 20, and 30 partial waves for the adiabatic $1^1A'$ (red solid lines), the adiabatic $1^1A''$ (green dashed lines), and nonadiabatic $2^1A'$ (blue dotted lines) reaction pathways, respectively.

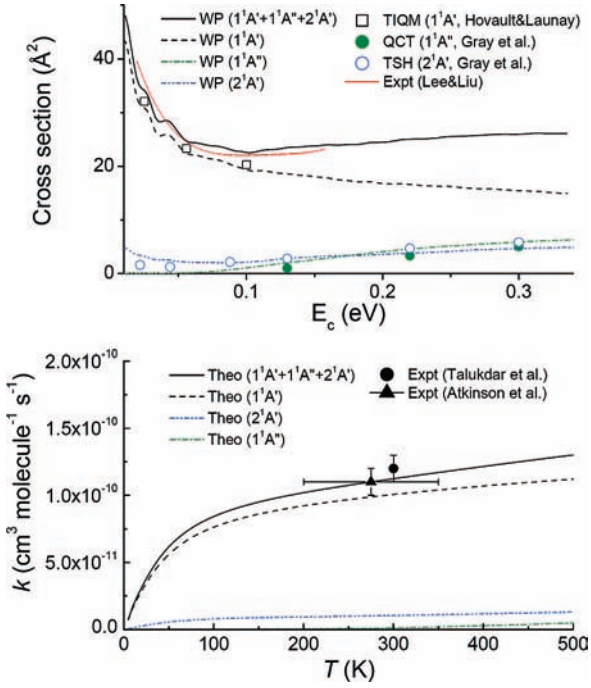

Figure 3. Energy dependence of total integral cross sections (upper panel) and temperature dependence of rate constants (lower panel). In the upper panel, our wave packet (WP) results are compared with the time-independent quantum mechanical (TIQM) results of Honvault and Launay[39] on the adiabatic $1^1A'$ pathway (open squares) and the QCT results of Gray et al.[59] for the adiabatic $1^1A''$ pathway and for the nonadiabatic $2^1A'$ pathway (closed and open circles, respectively). The experimental data of Lee and Liu[49] are given in a red dotted line.

his co-workers.[46,49] Quantitatively, the measured ICS for p-H_2 is compared in Figure 3 with our $j_i = 0$ results, and the agreement is almost perfect. This represents a substantial improvement of the previous QCT results of Gray et al.[59] (not shown), which underestimated the experimental curve. This improvement highlights the necessity of a quantum mechanical description of the title reaction.

In the same figure, the ICS obtained in this work is also compared with previous theoretical results. The agreement with the time-independent quantum mechanical (TIQM) work of Honvault and Launay[39] in the adiabatic $1^1A'$ channel is quite good, as shown. An equally good agreement was found for the $1^1A''$ pathway (not shown in the figure).[41] These agreements reaffirm the accuracy of our calculations. The comparison with the QCT results of Gray et al.[59] on the adiabatic $1^1A''$ pathway indicates that the quantum mechanical ICS is much larger than the QCT result near the threshold energies while agreeing reasonably well at higher energies. At the lowest energy point (0.13 eV), the quantum mechanical ICS (1.99 Å^2) is almost twice that of the QCT value (1.01 Å^2). This deviation, which has been noted before,[75] can almost certainly be attributed to tunneling effects, which were not accounted for in the QCT treatment. Finally, the contribution of the nonadiabatic $2^1A'$ pathway obtained from our quantum calculations is compared in the same figure with the trajectory surface hopping (TSH) results of Gray et al.[59] Overall, the agreement is quite reasonable, and it validates the TSH model for treating the nonadiabatic dynamics in this system. Quantitatively, however, the TSH data underestimate the quantum ICS at low collision energies but overestimate at high collision energies.

In the lower panel of Figure 3, contributions of the three reaction pathways to the rate constant were displayed. Again, they show the dominance of the $1^1A'$ ground adiabatic pathway in the title reaction. Between the two excited states, the contribution from the $2^1A'$ nonadiabatic dynamics is far larger than the contribution from the adiabatic $1^1A''$ pathway. This is due to the fact that the former has no threshold in the ICS, whereas the latter has a significant threshold. After including the excited-state contributions, the rate constant shows a near perfect agreement with experimental measurements,[15,17] further demonstrating the importance of excited-state dynamics. It is also clear from the figure that the rate constant depends only weakly on temperature.

In Figure 4, the percentage contributions of three pathways are displayed for both the total ICS (upper panel) and rate constant (lower panel). The figure confirms again the dominance of the ground $1^1A'$ state reaction pathway. At low energies, the $1^1A'$ pathway has a ~90% contribution to the total ICS, but it slowly decreases with the energy. On the other hand, the excited-state pathways become more and more important, contributing to the ICS as much as 40% (~20% for each state) at the highest collision energy investigated. The contribution of the $1^1A''$ pathway to the rate constant is negligibly small, although this state has a competitive contribution to the ICS at energies above its threshold. This is because the rate constant is largely determined by the cross section at low energies. However, the contribution of this state is expected to increase at higher temperatures. The nonadiabatic $2^1A'$ pathway has a ~10% contribution to the rate constant over the temperature range reported, and it has a mild temperature dependence.

B. State-to-State Integral Cross Section. In Figure 5, the product vibrational-state-resolved ICSs and their energy dependences are displayed for all three reaction pathways. They were obtained by summing state-to-state ICSs over all open rotational channels in a given vibrational manifold. The vibrationally resolved ICSs of the dominant $1^1A'$ pathway have no threshold and decrease monotonically with the collision before leveling off. The vibrational distribution is typically cold, characterized by a monotonically decaying population with the vibrational quantum number. These features derive from the insertion mechanism, for which the decay of the intermediate is largely statistical.

The vibrationally resolved ICSs in the adiabatic $1^1A''$ pathway behave completely differently. The ICSs all have significant thresholds and increase rapidly and smoothly with the collision

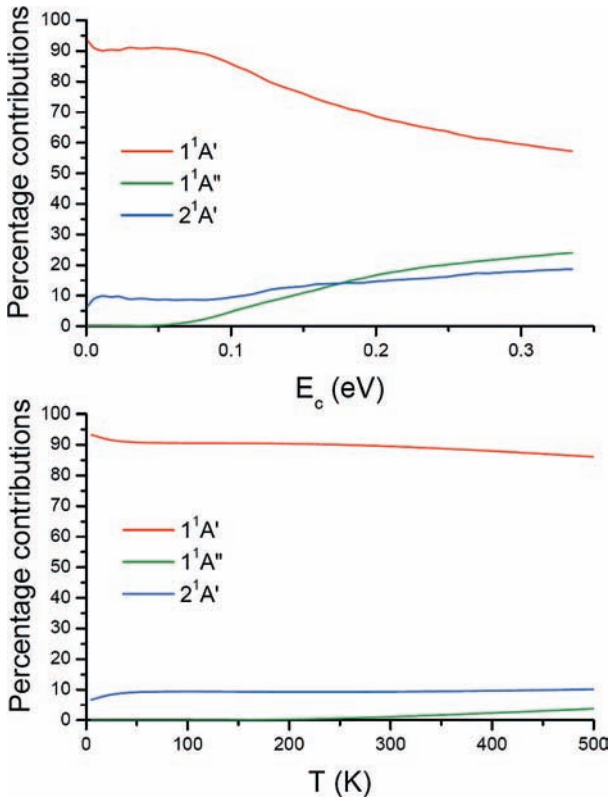

Figure 4. Percentage contributions of the three reaction pathways to the ICS (upper panel) and to the rate constant (lower panel).

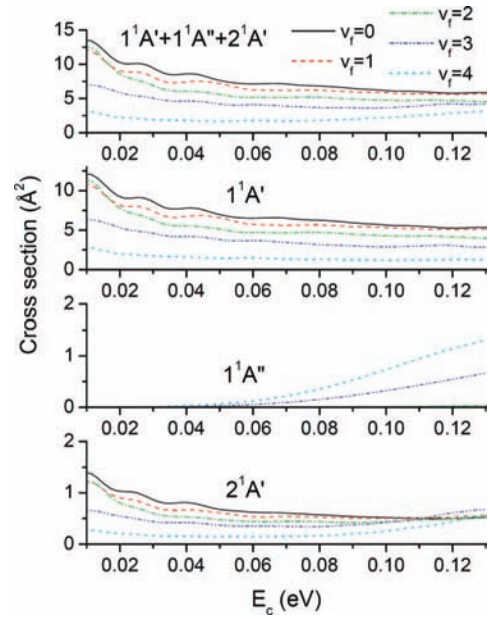

Figure 5. Total and individual product vibrational state distributions for the three reaction pathways and their dependence on the collision energy.

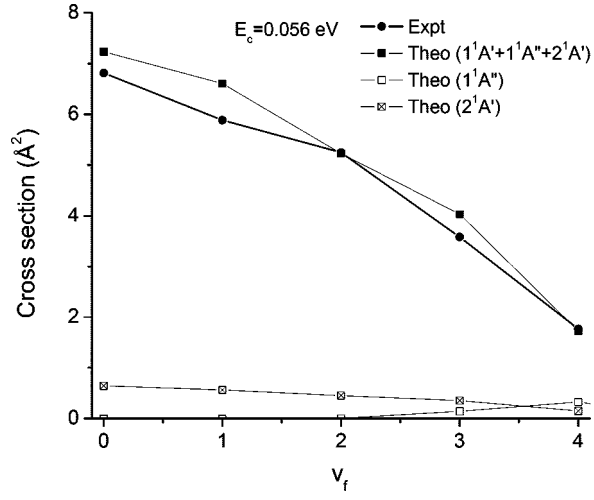

Figure 6. Comparison of the calculated and measured OH vibrational state distributions at the collision energy of 0.056 eV. The experimental data[25,41] have been normalized to the calculated distribution.

energy. Most strikingly, the vibrational distribution is highly inverted, with the largest population in the highest accessible vibrational ($v_f = 3, 4$) states. These features indicate clearly that the reaction is governed by the abstraction mechanism in which the incoming oxygen collides with H_2 near the collinear configuration. As a result, the departing OH product possesses a large amount of vibrational energy.

The vibrational distribution in the nonadiabatic $2^1A'$ pathway resembles that in the adiabatic $1^1A'$ pathway. This is particularly true at lower energies. At higher energies, however, all the vibrational states have nearly equal populations. At some energies, there is even some population inversion in the vibrational distribution. The reaction mechanism of the $2^1A'$ pathway is more complicated than the other two adiabatic pathways, since the reaction can take place only through nonadiabatic transitions to the $1^1A'$ state. At lower energies, most nonadiabatic transitions presumably take place near the entrance channel, and the reaction is primarily insertion-like. At higher energies, nonadiabatic transitions may occur after some time on the excited state, which could result in some signature of the abstraction mechanism.

In Figure 6, the calculated vibrational distribution at 0.056 eV is compared with the experimental measurement of Yang and co-workers.[25,41] The agreement is excellent. The inclusion of contributions from all the relevant pathways does not change the agreement in a significant way. As a result, this good agreement is essentially a reflection of the accuracy of the single-state quantum dynamics.[39,44]

In Figure 7, the product rotational state distributions for all the vibrational channels are compared with the experimental data at 0.056 eV.[25,41] The agreement is again very good, confirming the dominance of the insertion mechanism at this energy. In particular, the OH rotation is highly excited in all the vibrational manifolds, topping near the highest energetically accessible rotational states. As shown in the figure, the $1^1A''$ pathway is not quite open yet at this energy, and the contribution from the nonadiabatic $2^1A'$ pathway is also quite small.

It should be noted that some of the minor discrepancies in Figure 7 could be due to the approximate treatment of the spin and orbital angular momenta of the products. As shown by Alexander et al.,[76] the inclusion of these angular momenta as well as their couplings could result in slightly different product distributions.

The product rotational state distributions at higher collision energies (0.10 and 0.15 eV) are displayed in Figure 8. The overall shape of these distributions is similar to those shown in Figure 7, except they peak at higher rotational states because of the availability of extra energy. As shown in the figure, the rotational state distributions for the $1^1A''$ pathway are much less excited, due apparently to its collinear abstraction mechanism.

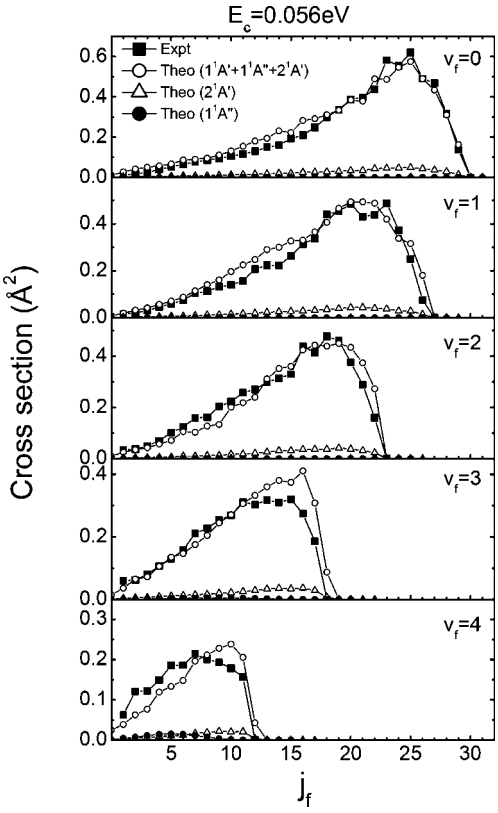

Figure 7. Comparison of the calculated and measured OH rotational state distributions at the collision energy of 0.056 eV. The experimental data[25,41] have been normalized to the calculated distributions.

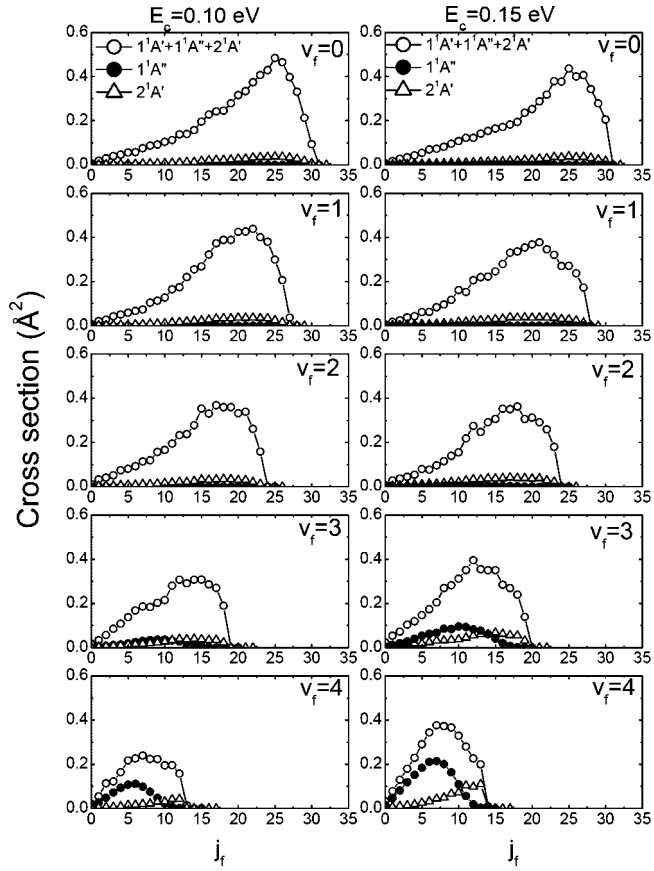

Figure 8. Calculated product rotational state distributions at 0.10 and 0.15 eV of collision energies.

They are typically Gaussian-shaped and peak at lower rotational states. The rotational state distributions for the $2^1A'$ pathway are similar to those for the $1^1A'$ pathway. Overall, the impact of the two excited-state pathways on the rotational state distribution is quite small. The only exception is in the highest vibrational states ($v_f = 3$, 4), where the rotational state distributions are overwhelmingly from the $1^1A''$ pathway.

C. Differential Cross Section. The DCSs, particularly the state-resolved DCSs, contain the most detailed information on the reaction mechanism and dynamics. Here, we focus on the total DCS because internal-state-resolved DCSs (not shown here) behave in a similar fashion except for more pronounced oscillations. In Figure 9, three-dimensional maps of the total DCSs are displayed as a function of both the center-of-mass scattering angle and collision energy for the three different reaction pathways. It is clear that the dominant $1^1A'$ pathway yields a near forward−backward symmetric DCS in all energies. This behavior stems from the insertion mechanism in which the reaction intermediate lives sufficiently long to lose its memory. The nonadiabatic $2^1A'$ pathway also results in a near forward−backward symmetric DCS, due largely to the fact that nonadiabatic transitions to the $1^1A'$ state PES occur in the entrance channel. On the other hand, the DCS for the $1^1A''$ pathway is strikingly different. Indeed, the product angular distribution is almost exclusively confined to the backward hemisphere at all collision energies, consistent with the direct abstraction mechanism on this excited state. These observations are consistent with earlier theoretical studies of the title reaction based on the QCT approach.[51,54,56] It is interesting to note that the DCSs of these two A′ pathways are very sensitive to the collision energy, whereas that of the A″ pathway is a smooth function of E_c.

To quantify the contributions of the three reaction pathways, we plot in Figure 10 the total DCS in three collision energies with the individual contributions. At the lowest collision energy (0.056 eV), contributions from the excited-state pathways are minimal and the DCS is almost solely from the ground state $1^1A'$ pathway. Because of its complex-forming nature, the DCS is clearly forward−backward symmetric. In the same figure, the experimental DCS[25,41] is also included. The overall agreement between the calculated and measured DCSs is reasonable, although the sharp peaks at the extremal angles of the calculated angular distribution are absent from the experimental data. This is likely due to the limitations in the experimental resolution.[29] There are also some oscillations in the calculated DCS, presumably stemming from quantum interference. Oscillations are commonly seen in quantum mechanical DCSs[39] but absent in those obtained by QCT calculations.[41,54,56]

At higher collision energies (0.10 and 0.15 eV), contributions of the excited-state pathways to the total DCS become increasingly important. While the nonadiabatic $2^1A'$ pathway generally raises the DCS at all scattering angles, it does not change the polarity of the angular distribution. On the other hand, the adiabatic $1^1A''$ pathway increases the bias toward the backward scattering direction, due apparently to its abstraction mechanism. The bias increases with the collision energy, stemming from the increasing weight of the adiabatic $1^1A''$ pathway. This observation is in good accord with the experimental observations[22] and previous QCT results on this reaction,[51,54,56] thus confirming the interpretation that the observed backward propensity is due to the participation of the excited-state abstraction pathway.[45,47,48]

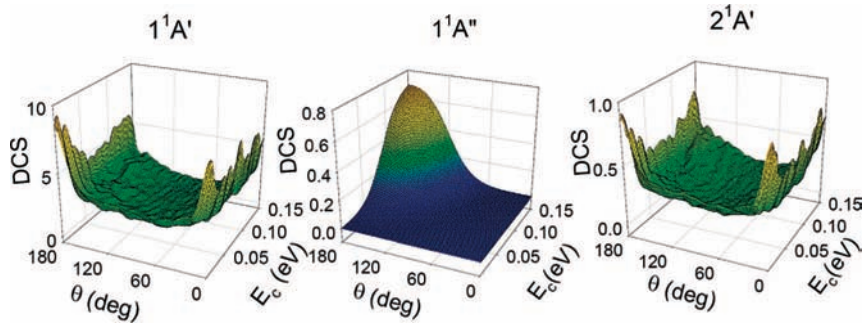

Figure 9. Three-dimensional plots of the DCSs from the three reaction pathways as a function of both the scattering angle and collision energy.

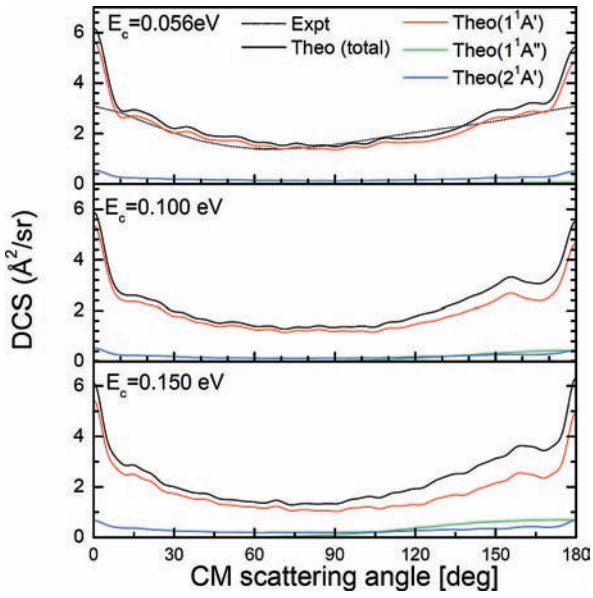

Figure 10. Total DCS and individual contributions from the three reaction pathways at three collision energies. The experimental data at 0.056 eV[25,41] have been normalized to the calculated DCS.

4. Conclusions

The title reaction provides an interesting prototype for studying scattering dynamics through multiple pathways with different reaction mechanisms. In particular, the barrierless $1^1A'$ adiabatic pathway is of a complex-forming nature, whereas the adiabatic $1^1A''$ pathway has an abstraction mechanism with a small barrier in the entrance channel. Finally, the nonadiabatic $2^1A'$ pathway accesses the product channel via nonadiabatic transitions to the ground $1^1A'$ state. Given the involvement of two hydrogen atoms, the dynamics is certainly of quantum mechanical nature. As a result, an accurate quantum mechanical characterization of all the relevant reaction pathways is highly valuable for a definitive elucidation of the reaction dynamics.

In this work, we report accurate quantum mechanical studies of all three reaction channels using the ab initio potential energy surfaces of Dobbyn and Knowles. The quantum dynamics was characterized by efficient wave packet methods based on the Chebyshev propagator. The calculation results provided an accurate account on the contributions of the three reaction pathways to the overall reaction and their dependence on the collision energy. They confirmed the conjecture that the reaction is dominated by the $1^1A'$ pathway throughout the energy range studied here. However, it is found that the nonadiabatic $2^1A'$ pathway also makes non-negligible contributions in almost all energies. Beyond the linear barrier of 0.1 eV, the two excited-state pathways become increasingly important. At the highest collision energy investigated in this work (0.3 eV), as much as 40% of the ICS comes from the two excited-state pathways. The participation of these excited-state pathways leads to a rise of the ICS with the collision energy, in quantitative agreement with the experimental observations of Liu and co-workers.

Our quantum dynamic results further showed that the dominant $1^1A'$ pathway is of insertion type, which yields rotationally hot and vibrational cold OH products with a nearly forward−backward symmetric angular distribution. On the other hand, the abstraction reaction in the $1^1A''$ pathway results in products with an inverted vibrational state distribution and low rotational excitation. In addition, its product angular distribution is confined in the backward hemisphere. Hence, the involvement of excited-state pathways can be detected in various measurable scattering attributes. In particular, the $1^1A''$ abstraction pathway leads to an increasingly backward-biased DCS as the collision energy increases, which deviates from the forward−backward symmetry characteristic of the insertion reaction in the $1^1A''$ pathway. This propensity is consistent with experimental observations of several groups. In addition, the $1^1A''$ pathway is also responsible for much cooler rotational state distributions in the highly excited vibrational states of the OH product. On the other hand, the effects of the $2^1A'$ pathway are mostly hidden, since its dynamic signature is essentially the same as the $1^1A'$ pathway.

For the rate constant up to 500 K, the $1^1A'$ pathway also dominates. However, the inclusion of the excited-state pathways is shown to significantly improve the agreement with experimental data. Interestingly, the contribution of the $1^1A''$ pathway is much smaller than that of the $2^1A'$ pathway because the latter has no reaction threshold.

Our quantum mechanical results also uncovered quantitative discrepancies in the QCT results stemming from the neglect of quantum effects. In particular, the QCT ICS for the $1^1A''$ pathway is found to substantially underestimate the quantum results, due apparently to tunneling over the small potential barrier in the entrance channel. On the other hand, the trajectory surface hopping results based on QCT are also shown to deviate from our quantum results, although the overall trend is well-reproduced. These observations underscore the necessity of an accurate quantum mechanical characterization of the reaction.

To summarize, the work reported here represents the most elaborate theoretical effort to date aimed at an accurate elucidation of the reaction dynamics in the prototypical reaction. The overall agreement with all available experimental data is excellent, underscoring the accuracy of the DK potentials and the quantum dynamics. Valuable insights are also gained from the dynamical studies on the participation of various reaction pathways, particularly the nonadiabatic $2^1A'$ pathway that has so far defied an accurate quantum mechanical study. Although

there are still many interesting issues to be addressed, our understanding of the reaction dynamics in this complex-forming reaction has reached an unprecedented level.

Acknowledgment. This work was supported by Department of Energy (DE-FG02-05ER15694). Stephen Gray is acknowledged for sending us the data published in ref 59, and Kopin Liu is thanked for several useful discussions. We are grateful to the continuous encouragement and support of Prof. George Schatz over the years.

References and Notes

(1) Anderson, G. *Annu. Rev. Phys. Chem.* **1987**, *38*, 489.
(2) Dixon-Lewis, G.; Williams, D. J. *Compr. Chem. Kinetics* **1977**, *17*, 1.
(3) Casavecchia, P. *Rep. Prog. Phys.* **2000**, *63*, 355.
(4) Ho, T.-S.; Hollebeek, T.; Rabitz, H.; Harding, L. B.; Schatz, G. C. *J. Chem. Phys.* **1996**, *105*, 10472.
(5) Schatz, G. C.; Papaioannou, A.; Pederson, L. A.; Harding, L. B.; Hollebeek, T.; Ho, T.-S.; Rabitz, H. *J. Chem. Phys.* **1997**, *107*, 2340.
(6) Dobbyn, A. J.; Knowles, P. J. *Mol. Phys.* **1997**, *91*, 1107.
(7) Dobbyn, A. J.; Knowles, P. J. *Faraday Disc.* **1998**, *110*, 247.
(8) Liu, K. *Annu. Rev. Phys. Chem.* **2001**, *52*, 139.
(9) Brouard, M.; O'Keeffe, P.; Vallance, C. *J. Phys. Chem. A* **2002**, *106*, 3629.
(10) Balucani, N.; Capozza, G.; Leonori, F.; Segoloni, E.; Casavecchia, P. *Int. Rev. Phys. Chem.* **2006**, *25*, 109.
(11) Aoiz, F. J.; Banares, L.; Herrero, V. J. *J. Phys. Chem. A* **2006**, *110*, 12546.
(12) Rackham, E. J.; Huarte-Larranaga, F.; Manolopoulos, D. E. *Chem. Phys. Lett.* **2001**, *343*, 356.
(13) Rackham, E. J.; Gonzalez-Lezana, T.; Manolopoulos, D. E. *J. Chem. Phys.* **2003**, *119*, 12895.
(14) Davidson, J. A.; Schiff, H. I.; Streit, G. E.; McAfee, J. R.; Scheltekopf, A. L.; Howard, C. *J. Chem. Phys.* **1977**, *67*, 5021.
(15) Atkinson, R.; Baulch, D. L.; Cox, R. A.; Hampson, R. F.; Kerr, J. A.; Troe, J. *J. Phys. Chem. Ref. Data* **1992**, *21*, 1125.
(16) Koppe, S.; Laurent, T.; Naik, P. D.; Volpp, H. R.; Wolfrum, J.; Arusi-Parpar, T.; Bar, I.; Rosenwaks, S. *Chem. Phys. Lett.* **1993**, *214*, 546.
(17) Talukdar, R. K.; Ravishankara, A. R. *Chem. Phys. Lett.* **1996**, *253*, 177.
(18) Buss, R. J.; Casavecchia, P.; Hirooka, T.; Sibener, S. J.; Lee, Y. T. *Chem. Phys. Lett.* **1981**, *82*, 386.
(19) Butler, J. E.; Jursich, G. M.; Watson, I. A.; Wiesenfeld, J. R. *J. Chem. Phys.* **1986**, *84*, 5365.
(20) Alexander, A. J.; Blunt, D. A.; Brouard, M.; Simons, J. P.; Aoiz, F. J.; Banares, L.; Fujimura, Y.; Tsubouchi, M. *Faraday Discuss.* **1997**, *108*, 375.
(21) Alexander, A. J.; Aoiz, F. J.; Banares, L.; Brouard, M.; Short, J.; Simons, J. P. *J. Phys. Chem. A* **1997**, *101*, 7544.
(22) Alagia, M.; Balucani, N.; Cartechini, L.; Casavecchia, P.; van Kleef, E. H.; Volpi, G. G.; Kuntz, P. J.; Sloan, J. J. *J. Chem. Phys.* **1998**, *108*, 6698.
(23) Ahmed, M.; Peterka, D. S.; Suits, A. G. *Chem. Phys. Lett.* **1999**, *301*, 372.
(24) Hsu, Y. T.; Liu, K.; Pederson, L. A.; Schatz, G. C. *J. Chem. Phys.* **1999**, *111*, 7921.
(25) Liu, X.; Lin, J. J.; Harich, S.; Schatz, G. C.; Yang, X. *Science* **2000**, *289*, 1536.
(26) Liu, X.; Lin, J. J.; Harich, S. A.; Yang, X. *J. Chem. Phys.* **2000**, *113*, 1325.
(27) Liu, X.; Lin, J. J.; Harich, S. A.; Yang, X. *Phys. Rev. Lett.* **2001**, *86*, 408.
(28) Liu, X.; Wang, C. C.; Harich, S. A.; Yang, X. *Phys. Rev. Lett.* **2002**, *89*, 133201.
(29) Yuan, K.; Cheng, Y.; Liu, X.; Harich, S.; Yang, X.; Zhang, D. H. *Phys. Rev. Lett.* **2006**, *96*, 103202.
(30) Peng, T.; Zhang, D. H.; Zhang, J. Z. H.; Schinke, R. *Chem. Phys. Lett.* **1996**, *248*, 37.
(31) Varandas, A. J. C.; Voronin, A. I.; Riganelli, A.; Caridade, P. J. S. B. *Chem. Phys. Lett.* **1997**, *278*, 325.
(32) Dai, J. *J. Chem. Phys.* **1997**, *107*, 4934.
(33) Alexander, A. J.; Aoiz, F. J.; Banares, L.; Brouard, M.; Herrero, V. J.; Simons, J. P. *Chem. Phys. Lett.* **1997**, *278*, 313.
(34) Balint-Kurti, G. G.; Gonzalez, A.; Goldfield, E. M.; Gray, S. K. *Faraday Discuss.* **1998**, *110*, 169.
(35) Gray, S. K.; Goldfield, E. M.; Schatz, G. C.; Balint-Kurti, G. G. *Phys. Chem. Chem. Phys.* **1999**, *1*, 1141.
(36) Hankel, M.; Balint-Kurti, G. G.; Gray, S. K. *J. Chem. Phys.* **2000**, *113*, 9658.
(37) Hankel, M.; Balint-Kurti, G. G.; Gray, S. K. *J. Phys. Chem. A* **2001**, *105*, 2330.
(38) Carroll, T. E.; Goldfield, E. M. *J. Phys. Chem.* **2001**, *105*, 2251.
(39) Honvault, P.; Launay, J.-M. *J. Chem. Phys.* **2001**, *114*, 1057.
(40) Aoiz, F. J.; Banares, L.; Castillo, J. F.; Brouard, M.; Denzer, W.; Vallance, C.; Honvault, P.; Launay, J.-M.; Dobbyn, A. J.; Knowles, P. J. *Phys. Rev. Lett.* **2001**, *86*, 1729.
(41) Aoiz, F. J.; Banares, L.; Castillo, J. F.; Herrero, V. J.; Martinez-Haya, B.; Honvault, P.; Launay, J.-M.; Liu, X.; Lin, J. J.; Harich, S.; Wang, C. C.; Yang, X. *J. Chem. Phys.* **2002**, *116*, 10692.
(42) Brandao, J.; Rio, C. M. A. *Chem. Phys. Lett.* **2003**, *377*, 523.
(43) Lin, S. Y.; Guo, H. *Chem. Phys. Lett.* **2004**, *385*, 193.
(44) Lin, S. Y.; Guo, H. *J. Chem. Phys.* **2008**, *129*, 124311.
(45) Che, D. C.; Liu, K. *J. Chem. Phys.* **1995**, *103*, 5164.
(46) Hsu, Y. T.; Wang, J. H.; Liu, K. *J. Chem. Phys.* **1997**, *107*, 2351.
(47) Hsu, Y. T.; Liu, K. *J. Chem. Phys.* **1997**, *107*, 1664.
(48) Hsu, Y. T.; Liu, K.; Pederson, L. A.; Schatz, G. C. *J. Chem. Phys.* **1999**, *111*, 7931.
(49) Lee, S.-H.; Liu, K. *J. Chem. Phys.* **1999**, *111*, 4351.
(50) Hermine, P.; Hsu, Y. T.; Liu, K. *Phys. Chem. Chem. Phys.* **2000**, *2*, 581.
(51) Balucani, N.; Casavecchia, P.; Aoiz, F. J.; Banares, L.; Castillo, J. F.; Herrero, V. J. *Mol. Phys.* **2005**, *103*, 1703.
(52) Kuntz, P. J.; Niefer, B. I.; Sloan, J. J. *J. Chem. Phys.* **1988**, *88*, 3629.
(53) Schatz, G. C.; Pederson, L. A.; Kuntz, P. J. *Faraday Discuss.* **1997**, *108*, 357.
(54) Aoiz, F. J.; Banares, L.; Castillo, J. F.; Herrero, V. J. *J. Chem. Phys.* **2000**, *113*, 5339.
(55) Alexander, A. J.; Aoiz, F. J.; Banares, L.; Brouard, M.; Simons, J. P. *Phys. Chem. Chem. Phys.* **2000**, *2*, 257.
(56) Aoiz, F. J.; Banares, L.; Castillo, J. F.; Herrero, V. J.; Martinez-Haya, B. *Phys. Chem. Chem. Phys.* **2002**, *4*, 4379.
(57) Drukker, K.; Schatz, G. C. *J. Chem. Phys.* **1999**, *111*, 2451.
(58) Gray, S. K.; Petrongolo, C.; Drukker, K.; Schatz, G. C. *J. Phys. Chem.* **1999**, *103*, 9448.
(59) Gray, S. K.; Balint-Kurti, G. G.; Schatz, G. C.; Lin, J. J.; Liu, X.; Harich, S.; Yang, X. *J. Chem. Phys.* **2000**, *113*, 7330.
(60) Takayanagi, T. *J. Chem. Phys.* **2002**, *116*, 2439.
(61) Althorpe, S. C.; Clary, D. C. *Annu. Rev. Phys. Chem.* **2003**, *54*, 493.
(62) Guo, H. *Rev. Comput. Chem.* **2007**, *25*, 285.
(63) Lin, S. Y.; Guo, H. *J. Phys. Chem. A* **2004**, *108*, 2141.
(64) Lin, S. Y.; Guo, H. *Phys. Rev. A* **2006**, *74*, 022703.
(65) Gray, S. K.; Balint-Kurti, G. G. *J. Chem. Phys.* **1998**, *108*, 950.
(66) Light, J. C.; Carrington, T., Jr. *Adv. Chem. Phys.* **2000**, *114*, 263.
(67) Kosloff, R. The Fourier Method In *Numerical Grid Methods and Their Applications to Schrodinger's Equation*; Cerjan, C., Ed.; Kluwer: Dordrecht, 1993.
(68) Condon, E. U.; Shortley, G. H. *The Theory of Atomic Spectra*; Cambridge: London, 1964.
(69) Zare, R. N. *Angular Momentum*; Wiley: New York, 1988.
(70) Corey, G. C.; Lemoine, D. *J. Chem. Phys.* **1992**, *97*, 4115.
(71) Corey, G. C.; Tromp, J. W. *J. Chem. Phys.* **1995**, *103*, 1812.
(72) Zhang, J. Z. H.; Miller, W. H. *J. Chem. Phys.* **1989**, *91*, 1528.
(73) Meijer, A. J. H. M.; Goldfield, E. M.; Gray, S. K.; Balint-Kurti, G. G. *Chem. Phys. Lett.* **1998**, *293*, 270.
(74) Lin, S. Y.; Guo, H. *J. Chem. Phys.* **2003**, *119*, 11602.
(75) Aoiz, F. J.; Banares, L.; Castillo, J. F.; Martinez-Haya, B.; de Miranda, M. P. *J. Chem. Phys.* **2001**, *114*, 8328.
(76) Alexander, M. H.; Rackham, E. J.; Manolopoulos, D. E. *J. Chem. Phys.* **2004**, *121*, 5221.

JP810948K